



## CHEMISTRY

## CO electroreduction on single-atom copper

Yuxuan Wang<sup>1†</sup>, Boyang Li<sup>2†</sup>, Bin Xue<sup>1,3†</sup>, Nicole Libretto<sup>4†</sup>, Zhenhua Xie<sup>5</sup>, Hao Shen<sup>1</sup>, Canhui Wang<sup>1</sup>, David Raciti<sup>6</sup>, Nebojsa Marinkovic<sup>5</sup>, Han Zong<sup>1</sup>, Wenjun Xie<sup>1</sup>, Ziyuan Li<sup>1</sup>, Guangye Zhou<sup>1</sup>, Jeff Vitek<sup>1</sup>, Jingguang G. Chen<sup>5</sup>, Jeffery Miller<sup>4</sup>, Guofeng Wang<sup>2\*</sup>, Chao Wang<sup>1\*</sup>

Electroreduction of carbon dioxide (CO<sub>2</sub>) or carbon monoxide (CO) toward C<sub>2+</sub> hydrocarbons such as ethylene, ethanol, acetate and propanol represents a promising approach toward carbon-negative electrosynthesis of chemicals. Fundamental understanding of the carbon–carbon (C–C) coupling mechanisms in these electrocatalytic processes is the key to the design and development of electrochemical systems at high energy and carbon conversion efficiencies. Here, we report the investigation of CO electroreduction on single-atom copper (Cu) electrocatalysts. Atomically dispersed Cu is coordinated on a carbon nitride substrate to form high-density copper–nitrogen moieties. Chemisorption, electrocatalytic, and computational studies are combined to probe the catalytic mechanisms. Unlike the Langmuir–Hinshelwood mechanism known for copper metal surfaces, the confinement of CO adsorption on the single-copper-atom sites enables an Eley–Rideal type of C–C coupling between adsorbed (\*CO) and gaseous [CO(g)] carbon monoxide molecules. The isolated Cu sites also selectively stabilize the key reaction intermediates determining the bifurcation of reaction pathways toward different C<sub>2+</sub> products.

## INTRODUCTION

Renewable energy-driven electroreduction of CO<sub>2</sub> represents a promising approach toward artificial carbon recycling (1, 2). Electrolytes of high alkalinity are known to favor C–C coupling, a key step toward value-added C<sub>2+</sub> hydrocarbon products such as ethylene, ethanol, acetate, and *n*-propanol (3, 4). However, CO<sub>2</sub> dissolves in aqueous electrolytes to form carbonic acid (H<sub>2</sub>CO<sub>3</sub>), which reacts with hydroxide and causes degradation of the electrolyte (5). This challenge can be circumvented by sequential electroreduction of CO<sub>2</sub> to CO and then CO to C<sub>2+</sub> (6–12). Conversion of CO<sub>2</sub> to CO can be carried out in a bicarbonate buffer (e.g., KHCO<sub>3</sub>), for which >90% Faradaic efficiency (FE) toward CO has been demonstrated using metal catalysts such as Au (13–15) and Ag (16) or single-metal–atom (17, 18) electrocatalysts. Meanwhile, the electroreduction of CO can be done using high-alkalinity electrolytes to take advantage of the enhanced C<sub>2+</sub> selectivities (10, 19–24).

Metallic copper has been the sole monometallic catalyst known for favoring C<sub>2+</sub> products in CO<sub>2</sub> and CO electroreduction (6, 25, 26). The rate of C<sub>2+</sub> production is typically limited by the C–C coupling step between adjacent \*CO(H) adsorbates, which is sensitive to the surface structure of Cu (19, 20, 26). On Cu(100) and (110), the surface atoms with a fourfold symmetry are able to accommodate and stabilize the transition state of C–C coupling between two bridge-adsorbed \*CO (8, 27–31). Such \*CO–\*CO dimerization is mediated by electron transfer and has a lower energy barrier than C–C coupling after a hydrogenation step, e.g., between \*CO and

\*CHO (or \*COH). The latter likely takes place at relatively high overpotentials on Cu(111) (32, 33), although \*CO–\*CO dimerization has also been cited to account for the selective reduction of CO to acetate on this type of metal surface (31, 34). Nevertheless, the understanding of CO<sub>2</sub>/CO reduction pathways toward C<sub>2+</sub> products thus far is largely limited to the Langmuir–Hinshelwood (L-H) mechanism, which usually requires high coverages of adsorbing intermediates (35). While Cu binds to \*CO relatively weakly, other transition metals such as Pt and Pd bind to CO too strongly and suffer from CO poisoning (36). Advanced electrocatalytic materials with alternative C–C coupling mechanisms and enhanced selectivity toward a specific C<sub>2+</sub> product remain to be developed for CO<sub>2</sub>/CO reduction electrocatalysis.

Here, we report a single-copper-atom electrocatalyst for selective reduction of CO to acetate (Fig. 1). By copolyolysis of copper chloride (CuCl<sub>2</sub>) and urea (see Materials and Methods for details), atomically dispersed Cu was supported on nonstoichiometric carbon nitride (denoted as Cu<sub>1</sub>@*n*-C<sub>3</sub>N<sub>4</sub>) and stabilized via copper–nitrogen coordination (Fig. 2A). The Cu<sub>1</sub>@*n*-C<sub>3</sub>N<sub>4</sub> electrocatalyst exhibited high activity for selective reduction of CO to multicarbon products, with the overall FE toward C<sub>2+</sub> (FE<sub>C<sub>2+</sub></sub>) reaching 74%. In particular, acetate is the dominant product with FE<sub>acetate</sub> achieving ~50%, which surpasses many known electrocatalysts for acetate production under similar conditions (table S1). A

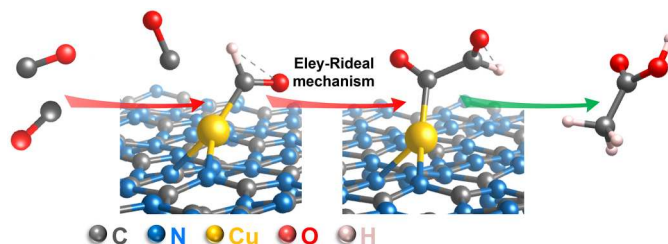


**Fig. 1. Scheme of concept.** Illustration of the E-R mechanism for CO electroreduction on Cu<sub>1</sub>@*n*-C<sub>3</sub>N<sub>4</sub>.

<sup>1</sup>Department of Chemical and Biomolecular Engineering and Ralph O'Connor Sustainable Energy Institute, Johns Hopkins University, Baltimore, MD 21218, USA.

<sup>2</sup>Department of Mechanical Engineering and Materials Science, University of Pittsburgh, Pittsburgh, PA 15261, USA. <sup>3</sup>Department of Chemistry, College of Food Science and Technology, Shanghai Ocean University, Shanghai 201306, China.

<sup>4</sup>Davidson School of Chemical Engineering, Purdue University, West Lafayette, IN 47907, USA. <sup>5</sup>Department of Chemical Engineering, Columbia University, New York City, NY 10027, USA. <sup>6</sup>Materials Science and Engineering Division, National Institute of Standards and Technology, Gaithersburg, MD 20899, USA.

\*Corresponding author. Email: chaowang@jhu.edu (C.W.); guw8@pitt.edu (G.W.)

†These authors contributed equally to this work.

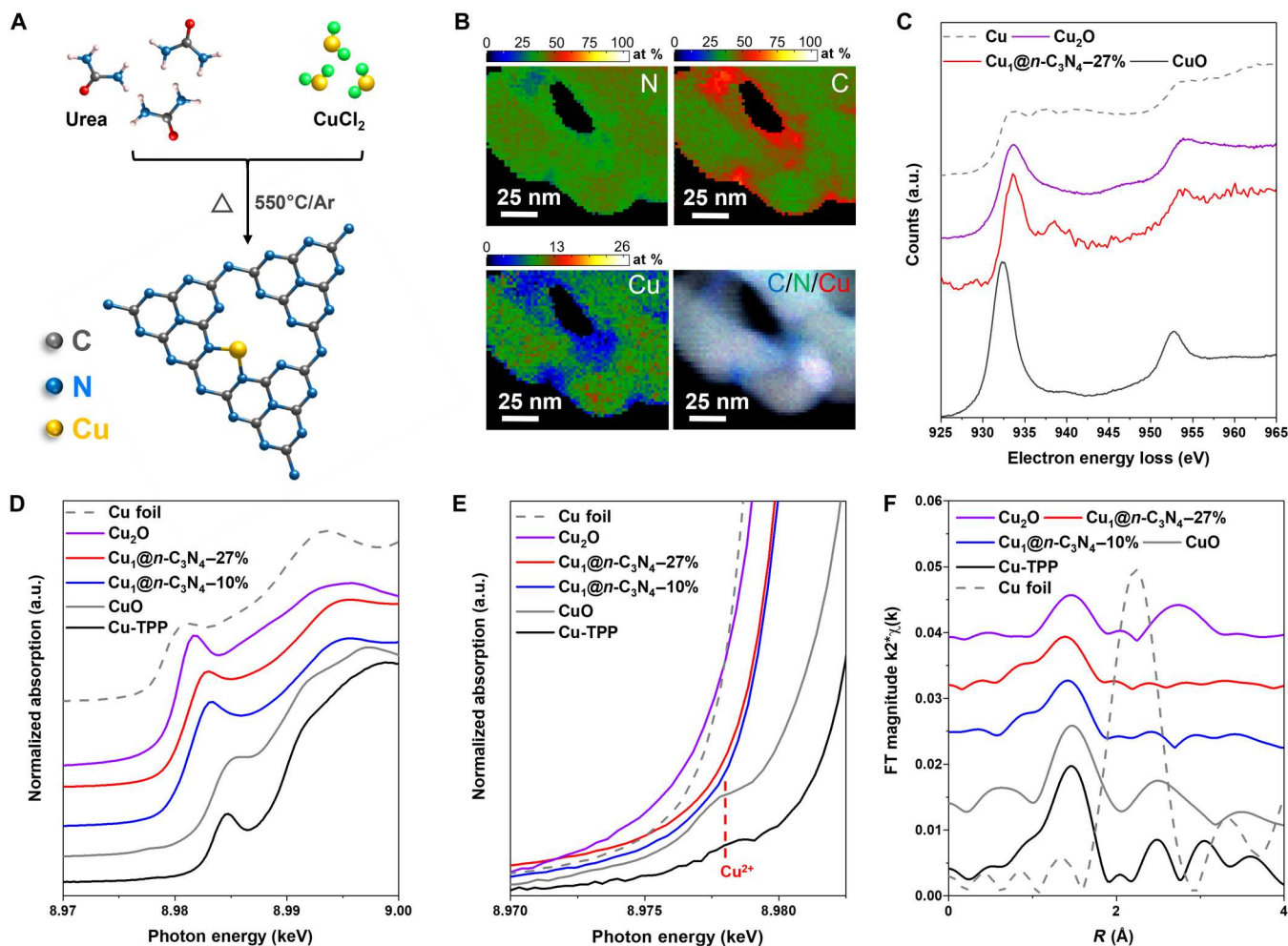


**Fig. 2. Synthesis and characterization.** (A) Scheme for the synthesis of  $\text{Cu}_1@n\text{-C}_3\text{N}_4$ . (B) EELS-based elemental mapping (color contoured in atomic %) on  $\text{Cu}_1@n\text{-C}_3\text{N}_4$ -27%. (C) EELS spectra of  $\text{Cu}_1@n\text{-C}_3\text{N}_4$ -27% and the references (Cu,  $\text{Cu}_2\text{O}$ , and CuO). (D and E) XANES and (F) EXAFS spectra of  $\text{Cu}_1@n\text{-C}_3\text{N}_4$ -27%,  $\text{Cu}_1@n\text{-C}_3\text{N}_4$ -10%, and the references including  $\text{Cu}_2\text{O}$ , CuO, Cu-TPP, and Cu foil. a.u., arbitrary units.

combination of kinetic study depending on CO partial pressure and Tafel slope analysis revealed that a unique Eley-Rideal (E-R) mechanism accounts for C–C coupling on the isolated copper sites. This mechanism was further corroborated by performing density functional theory (DFT) calculations, which illustrated the distinct adsorption configurations of key reaction intermediates determining the C–C coupling mechanism and the following bifurcation of reaction pathways toward different  $\text{C}_{2+}$  products.

## RESULTS

### Synthesis and characterization of Cu single-atom electrocatalysts

Two Cu single-atom electrocatalysts (SAECs) were prepared with 27 and 10 weight % (wt %) of metal loading (denoted as  $\text{Cu}_1@n\text{-C}_3\text{N}_4$ -27% and  $\text{Cu}_1@n\text{-C}_3\text{N}_4$ -10%), for which the element compositions were characterized using electron energy-loss spectroscopy (EELS) and inductively coupled plasma atomic emission spectroscopy (fig. S1). Pristine  $\text{C}_3\text{N}_4$  derived from the pyrolysis of urea in the absence of  $\text{CuCl}_2$  was used as a control (37). The high metal loading in

$\text{Cu}_1@n\text{-C}_3\text{N}_4$ -27% is in line with the theoretical capacity (26.3 wt %) of graphitic carbon nitride ( $g\text{-C}_3\text{N}_4$ ) if one Cu atom is presumably anchored on each unit cell (fig. S2), albeit that the C:N atomic ratios in the  $n\text{-C}_3\text{N}_4$  substrates are off the stoichiometry of  $g\text{-C}_3\text{N}_4$  (56:44 and 47:52 for  $\text{Cu}_1@n\text{-C}_3\text{N}_4$ -10% and  $\text{Cu}_1@n\text{-C}_3\text{N}_4$ -27%, respectively). X-ray diffraction (XRD) patterns of these materials show typical peaks of  $\text{C}_3\text{N}_4$ , and no features are found to be associated with copper metal or copper oxides (fig. S3). The strongest peak at  $27.5^\circ$  can be assigned to the (002) lattice plane of  $g\text{-C}_3\text{N}_4$ , corresponding to a d spacing of 0.323 nm between the stacked graphitic layers of  $\text{C}_3\text{N}_4$ . The absence of aggregated copper species is confirmed by both low- and high-resolution transmission electron microscopy (TEM) imaging (figs. S4 and S5). High-angle annual dark-field scanning TEM (HAADF-STEM) images show that the majority of Cu species is dispersed as individual atoms. The bright-field STEM images show a layered structure with an interlayer spacing of  $\sim 0.33$  nm, corresponding to the (002) lattice planes of  $\text{C}_3\text{N}_4$  as also resolved from the XRD analysis (fig. S6).

Elemental mapping based on STEM-EELS spectral imaging analysis shows uniformly distributed Cu species at high densities

on the  $n\text{-C}_3\text{N}_4$  substrate (Fig. 2B). Line profile analysis suggests that the distribution of Cu is more tightly correlated to N than C, indicating the preferential anchoring of Cu at the nitrogen sites on the substrate (fig. S7). The EELS spectra for  $\text{Cu}_1@n\text{-C}_3\text{N}_4$  exhibit white line features with onsets at  $\sim 933$  and  $\sim 953$  eV. Compared to the various references including Cu,  $\text{Cu}_2\text{O}$ , and  $\text{CuO}$ , these features can be assigned to the  $L_3$  and  $L_2$  absorption edges of  $\text{Cu}^{1+}$ , suggesting an oxidation state of +1 for the copper species in the SAECs (Fig. 2C). This finding is corroborated by x-ray photoelectron spectroscopy (XPS) measurements (fig. S8), as evidenced from the absence of the satellite peak in Cu 2p XPS spectrum and the 916.8 eV ( $L_2M_{45}M_{45}$ ) peak in Cu Auger spectrum which are characteristic of  $\text{Cu}^{2+}$ . The N 1s XPS spectra were also fitted to compare the coordination environments between  $g\text{-C}_3\text{N}_4$  and  $\text{Cu}_1@n\text{-C}_3\text{N}_4\text{-27\%}$  (fig. S9). Notably,  $\text{Cu}_1@n\text{-C}_3\text{N}_4\text{-27\%}$  exhibits a much more pronounced feature associated with the tri-coordinated N ( $M\text{-N-C}_2$ ) than for  $g\text{-C}_3\text{N}_4$ , consistent with the expectation for Cu–N coordination (38).

Atomic structure of the Cu SAECs was resolved by performing x-ray absorption spectroscopy (XAS) measurements. X-ray absorption near-edge structure (XANES) regions of both  $\text{Cu}_1@n\text{-C}_3\text{N}_4\text{-27\%}$  and  $\text{Cu}_1@n\text{-C}_3\text{N}_4\text{-10\%}$  exhibit onsets at 8.982 keV, which resembles the case for  $\text{Cu}_2\text{O}$  but is distinct from Cu (8.981 keV) and  $\text{CuO}$  (8.985 keV) (Fig. 2D) (39, 40). The XANES spectra of  $\text{Cu}_1@n\text{-C}_3\text{N}_4$  are also distinct from Cu(II) tetraphenylporphyrin (Cu-TPP), an organometallic compound with fourfold Cu–N coordination (fig. S10), by showing no pre-edge feature around 8.978 keV, with the latter being characteristic of  $\text{Cu}^{2+}$  (Fig. 2E) (41). The XANES analysis is thus consistent with EELS and confirms the 1+ oxidation state of Cu in the SAECs. The local atomic coordination around the Cu centers was inferred by fitting the extended x-ray adsorption fine structure (EXAFS) spectra (Fig. 2F). The first-shell fit demonstrates that  $\text{Cu}_1@n\text{-C}_3\text{N}_4\text{-27\%}$  and  $\text{Cu}_1@n\text{-C}_3\text{N}_4\text{-10\%}$  contain 1.8 and 1.7 Cu–N bonds, respectively, with a bond length of 1.91 Å (table S2; see the details of fitting in fig. S12). This short bonding distance is in line with Cu–N observed in Cu-TPP (1.98 Å), whereas typical Cu–O bonding distances in reference oxides ( $\text{CuO}$  and  $\text{Cu}_2\text{O}$ ) exceed 2.00 Å. No Cu–Cu bond was observed, confirming the single-atom dispersion of Cu in the SAECs.

### Electrocatalytic studies for CO reduction

The electroreduction of CO was measured using a gas-diffusion electrode (GDE) cell and 1 M KOH as the flowing electrolyte (fig. S13, A and B) (42, 43). The products derived from  $\text{Cu}_1@n\text{-C}_3\text{N}_4\text{-27\%}$  are mainly composed of  $\text{C}_{2+}$  hydrocarbons throughout the investigated potential range [from  $-0.5$  to  $-1.0$  V versus reversible hydrogen electrode (RHE); the same potential scale is used in the following discussion unless otherwise specified], which are dominated by acetate but still contain a trace amount of methane at potentials more negative than  $-0.6$  V (Fig. 3A and fig. S13C).  $\text{FE}_{\text{CH}_3\text{COO}^-}$  reaches 46% at  $-0.5$  V and persists at more negative potentials, with the maximum, 48%, recorded at  $-0.8$  V (Fig. 3B). Ethylene also appears at  $-0.5$  V, with a relatively low FE ( $\text{FE}_{\text{CH}_2\text{CH}_2}$ ) of 3%. Ethanol and  $n$ -propanol are present in the products obtained at potentials more negative than  $-0.7$  V, with corresponding  $\text{FE}_{\text{C}_2\text{H}_5\text{OH}}$  and  $\text{FE}_{\text{C}_3\text{H}_7\text{OH}}$  found to be at  $\sim 8$  and  $\sim 6\%$ , respectively. The FE toward methane ( $\text{FE}_{\text{CH}_4}$ ) is merely 4% at most as observed at  $-1.0$  V. Noticeably, the high activity and selectivity of  $\text{Cu}_1@n\text{-C}_3\text{N}_4\text{-27\%}$

persist through elongated operations. In a chronopotentiometric stability test at  $60 \text{ mA/cm}^2$ , the overpotential was quite stable throughout a period of 24 hours, and  $\text{FE}_{\text{CH}_3\text{COO}^-}$  only changed slightly from 48% at the beginning to 44% at the end (Fig. 3C). Compared to the previously reported electrocatalytic performances of Cu nanocrystals for CO reduction, the Cu SAECs behave more similar to  $\text{Cu}(111)$  nanosheets in terms of selective production of acetate, as compared to Cu nanocubes [with (100) dominated surface] that favors ethylene production (34). However, the discrete, namely, absence of continual copper-atom ensembles, and cationic (+1, versus metallic  $\text{Cu}^0$ ) nature of the active sites suggests a different catalytic mechanism toward the same  $\text{C}_2$  product, acetate, on the Cu SAECs.

We have further compared  $g\text{-C}_3\text{N}_4$  (fig. S14) and  $\text{Cu}_1@n\text{-C}_3\text{N}_4\text{-10\%}$  (fig. S15) with  $\text{Cu}_1@n\text{-C}_3\text{N}_4\text{-27\%}$  for CO reduction. At  $-1.0$  V,  $\text{Cu}_1@n\text{-C}_3\text{N}_4\text{-27\%}$  delivers the highest total current density per geometric area of the electrode ( $J_{\text{tot}}$ ), which achieves  $104 \text{ mA/cm}^2$  (Fig. 3D). At this potential,  $\text{Cu}_1@n\text{-C}_3\text{N}_4\text{-10\%}$  and  $g\text{-C}_3\text{N}_4$  deliver 63 and  $14 \text{ mA/cm}^2$ , respectively. Similar trend exhibits in the current density of CO reduction ( $J_{\text{CO}}$ ), which reads at 83.9 and  $28.1 \text{ mA/cm}^2$  at  $-1.0$  V for  $\text{Cu}_1@n\text{-C}_3\text{N}_4\text{-27\%}$  and  $\text{Cu}_1@n\text{-C}_3\text{N}_4\text{-10\%}$ , respectively (Fig. 3E). No CO reduction product in substantial amount but  $\text{H}_2$  was obtained from the control experiment with  $g\text{-C}_3\text{N}_4$  (fig. S14). Moreover, the selectivity also correlates tightly to the Cu loading. For example,  $\text{FE}_{\text{CH}_3\text{COO}^-}$  reads at 0, 14, and 48% at  $-0.8$  V for the three catalysts, corresponding to  $J_{\text{CH}_3\text{COO}^-}$  of 0, 7.1, and  $32.9 \text{ mA/cm}^2$ , respectively (Fig. 3F; also see figs. S14 and S15 for more electrocatalytic results of  $\text{Cu}_1@n\text{-C}_3\text{N}_4\text{-10\%}$  and  $g\text{-C}_3\text{N}_4$ ). The consistent trends of  $\text{Cu}_1@n\text{-C}_3\text{N}_4\text{-27\%} > \text{Cu}_1@n\text{-C}_3\text{N}_4\text{-10\%} > g\text{-C}_3\text{N}_4$  for both current density and FE indicates that the atomically dispersed Cu is not only the active site for activation of CO but also accounts for C–C coupling and restriction of the consequent reaction pathway toward a specific  $\text{C}_2$  product. This is congruent with the control experiment performed on Cu nanoparticles supported on  $\text{C}_3\text{N}_4$ , which does not show comparable performance with the Cu SAECs for electroreduction of CO to acetate (fig. S16). Moreover, electrocatalytic studies using isotope-labeled  $^{13}\text{CO}$  confirmed that both carbon atoms in the acetate product were derived from the reduction of carbon monoxide (figs. S17 and S18).

### Active sites and kinetic studies

The assignment of single-atom Cu as the active site is corroborated by performing diffuse reflectance infrared Fourier transform spectroscopy (DRIFTS) and CO stripping voltammetry analyses. In the DRIFTS spectra collected on  $\text{Cu}_1@n\text{-C}_3\text{N}_4\text{-27\%}$  and  $\text{Cu}_1@n\text{-C}_3\text{N}_4\text{-10\%}$  with CO preabsorbed at room temperature, a peak appears at  $2,098 \text{ cm}^{-1}$ , which is absent in the case of  $g\text{-C}_3\text{N}_4$  (Fig. 4A). This feature can be assigned to the stretching of C=O bond in linearly absorbed  $^*\text{CO}$  (18, 44, 45). In line with the observations from DRIFTS, the CO stripping voltammograms (recorded at room temperature in 0.1 M KOH; see the experimental details in Materials and Methods) recorded on  $\text{Cu}_1@n\text{-C}_3\text{N}_4\text{-27\%}$  and  $\text{Cu}_1@n\text{-C}_3\text{N}_4\text{-10\%}$  exhibit a peak at 0.28 V, which is not seen for  $g\text{-C}_3\text{N}_4$  (Fig. 4B). The peak intensity integrated from the CO stripping voltammograms increases with metal loading (fig. S19), signaling that the observed  $^*\text{CO}$  features are indeed associated with the uniformly distributed single-atom Cu sites. Noticeably, the previous studies of temperature-programmed CO desorption show that  $^*\text{CO}$  desorbs

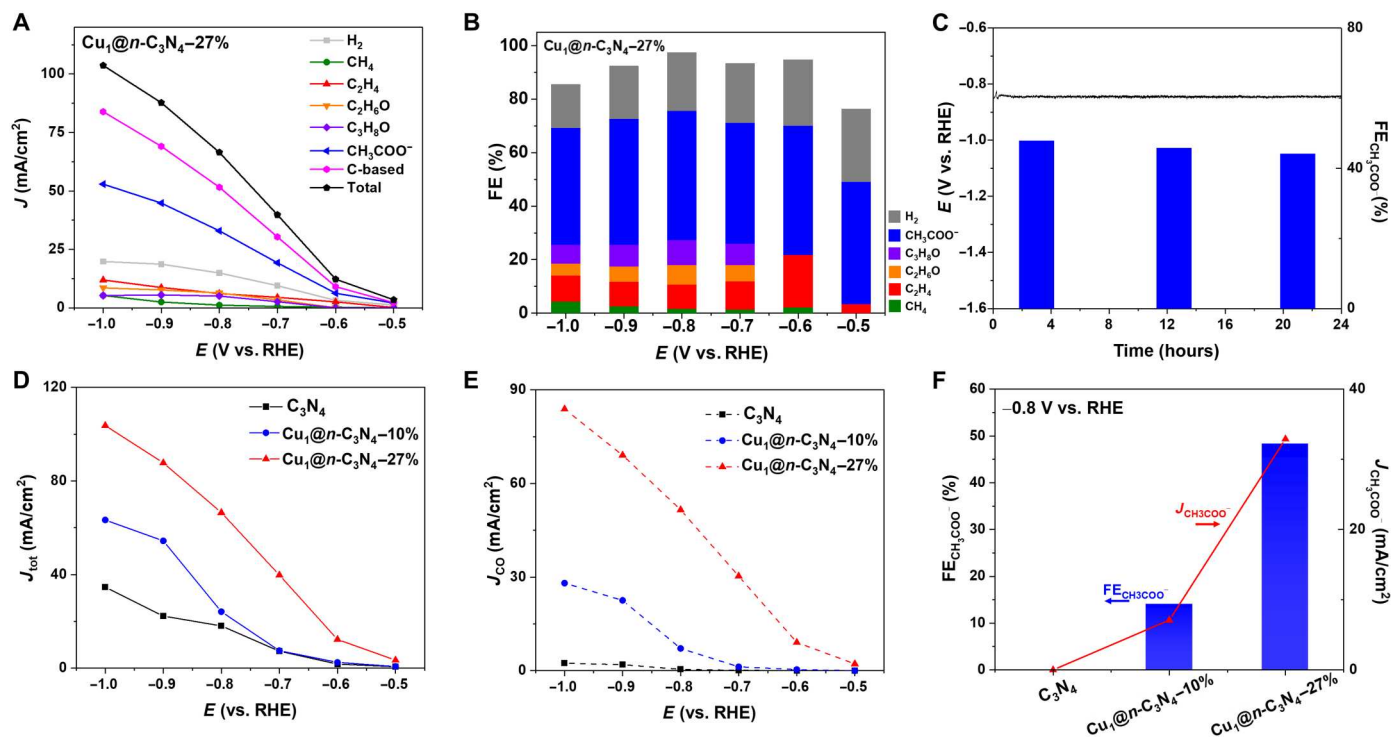


**Fig. 3. Electrochemical performance.** (A) Partial current densities, (B) FEs, and (C) stability test of  $\text{Cu}_1@n\text{-C}_3\text{N}_4\text{-27\%}$ . Comparison of (D) total current density ( $J_{\text{tot}}$ ), (E) partial current density for CO reduction ( $J_{\text{CO}}$ ), and (F) FE ( $\text{FE}_{\text{CH}_3\text{COO}^-}$ ) and current density ( $J_{\text{CH}_3\text{COO}^-}$ ) for acetate at  $-0.8$  V among  $g\text{-C}_3\text{N}_4$ ,  $\text{Cu}_1@n\text{-C}_3\text{N}_4\text{-10\%}$ , and  $\text{Cu}_1@n\text{-C}_3\text{N}_4\text{-27\%}$ .

from metallic Cu surfaces below or at room temperature (31, 46). Meanwhile, no such features were observed in our control experiments with the  $\text{C}_3\text{N}_4$ -supported Cu nanoparticles (fig. S20). Thus, atomically dispersed Cu sites in the SAECs are believed to have distinct adsorption properties from their metallic counterparts and thereby give rise to dissimilar catalytic mechanisms for CO reduction. As to be shown below by computational simulations, such a difference is corroborated by the much stronger binding of CO on the single-atom Cu sites than on continuous Cu surfaces.

Stability of the Cu SAECs was also revealed by in situ XAS studies, which showed nearly no change in either XANES or EXAFS spectra under reaction conditions (Fig. 4, C and D and fig. S21). The structural fitting parameters derived from the in situ EXAFS spectra are included in table S2. We found that the coordination number of Cu in  $\text{Cu}_1@n\text{-C}_3\text{N}_4$  increased from 1.7 to 1.8 measured ex situ (Fig. 1F, protected with Kapton tape and kept from exposure to air) to 2.7 to 2.8 under the CO reduction reaction condition. Such a difference can be attributed to the adsorption of CO, as the Cu–N (1.91 Å) and Cu–C (1.78 Å for Cu–\*CO) bonding involved in the  $\text{Cu}_1@n\text{-C}_3\text{N}_4$  electrocatalysts are nearly indiscernible in EXAFS. Because of the strong Cu–\*CO binding (as predicted from the DFT calculations and confirmed with the above chemisorption analysis), the coverage of \*CO on the single-atom Cu sites is expected to be high (near one monolayer) during the reaction. These adsorbate-induced changes in coordination number have also been observed in the previous in situ XAS studies of transition metals (such as Pt and Pd) that bind strongly to CO (47, 48).

Given with the clear indication of single-atom Cu being the active sites, we then turned our effort to find out the rate-

determining step (RDS) of CO reduction on such sites. For that purpose, we performed kinetic analysis of the reaction order with respect to CO and the Tafel slope in terms of  $J_{\text{CH}_3\text{COO}^-}$ . In the former case, the electroreduction of CO was measured at various CO partial pressures ( $P_{\text{CO}}$ ) at  $-0.6$  V. While the total current densities remain quite consistent,  $J_{\text{H}_2}$  decreases from 11.5  $\text{mA}/\text{cm}^2$  at  $P_{\text{CO}} = 0$  to 4.6  $\text{mA}/\text{cm}^2$  at  $P_{\text{CO}} = 1$  atm, corresponding to increase in CO reduction current density from 0 to 10.1  $\text{mA}/\text{cm}^2$  (Fig. 4D). Product distribution shares a similar trend, namely, decreasing  $\text{FE}_{\text{H}_2}$  and increasing  $\text{FE}_{\text{C}_2}$  with  $P_{\text{CO}}$  (Fig. 4E). We have further analyzed the reaction order ( $n$ ) with respect to CO for the reduction of CO to acetate, the major  $\text{C}_2$  product.  $n$  is found to exhibit divergent values at different  $P_{\text{CO}}$  values (Fig. 4F). In the low- $P_{\text{CO}}$  region (0 to 0.15 atm), the rate of acetate production is nearly first order with respect to CO. The reaction seems to approach saturation at  $P_{\text{CO}} > 0.3$  atm, and the rate of acetate production becomes weakly dependent on the CO concentration, where  $n$  drops to 0.15. Between these two extremes is obviously a transitional region with an intermediate  $n$  of 0.49. In line with the observations in terms of reaction orders, the slope ( $\eta$ ) derived from the Tafel plot for  $J_{\text{CH}_3\text{COO}^-}$  also diverges at high and low  $P_{\text{CO}}$  values, determined to be  $-123$  and  $-406$  mV per decade at  $P_{\text{CO}} = 1$  and 0.15 atm, respectively (Fig. 4G).

Comparing these kinetic parameters to those expected for the different RDSs of  $\text{C}_{2+}$  product formation (table S3) (49, 50), the high- $P_{\text{CO}}$  case with nearly zero reaction order and a Tafel slope of  $-123$  mV per decade for acetate production indicate that the reaction rate is limited by the hydrogenation of \*CO to \*CHO (or

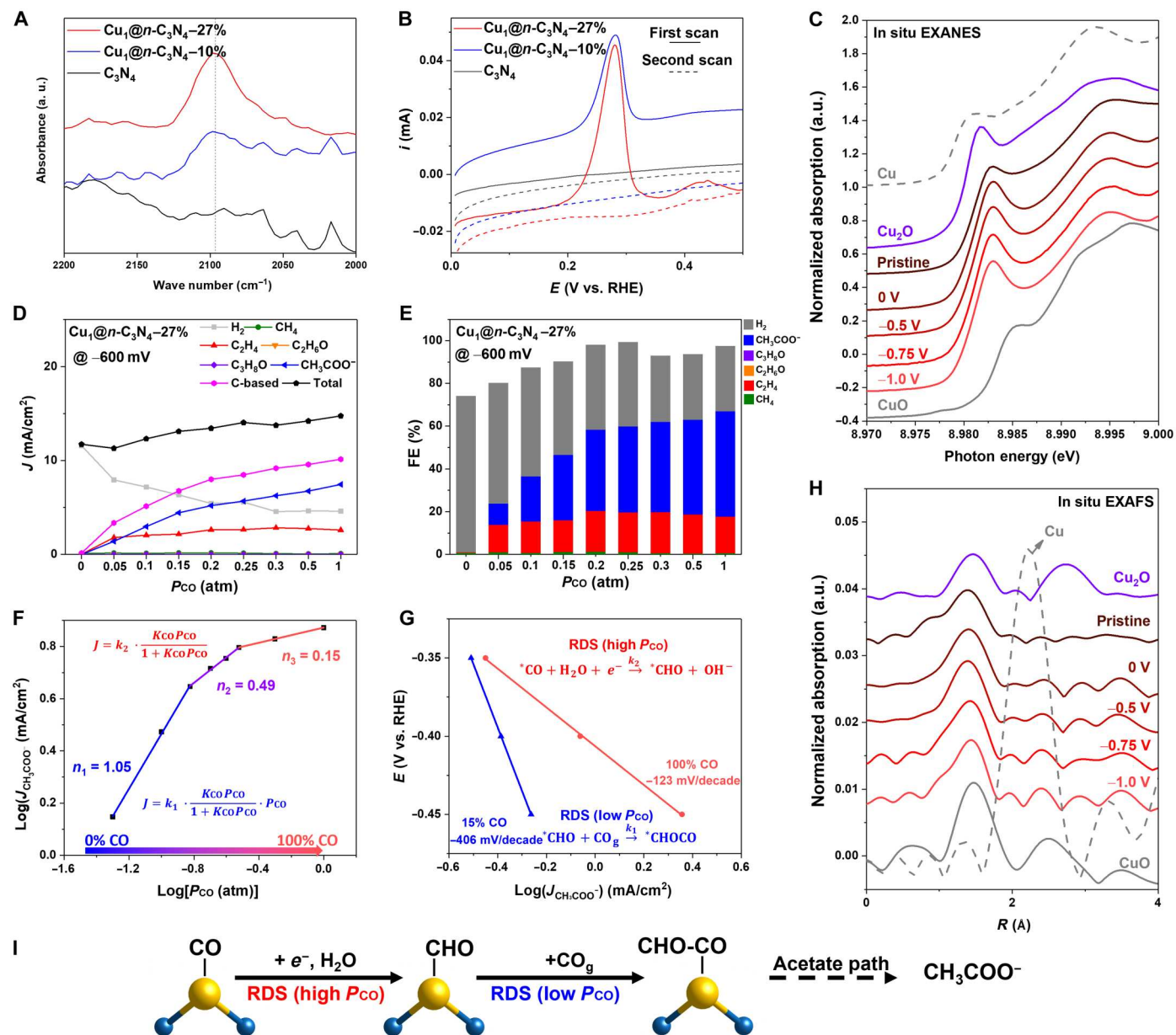


**Fig. 4. Active sites and kinetic studies.** (A) DRIFTS spectra and (B) CO stripping voltammograms of Cu<sub>1</sub>@n-C<sub>3</sub>N<sub>4</sub>-27%, Cu<sub>1</sub>@n-C<sub>3</sub>N<sub>4</sub>-10%, and g-C<sub>3</sub>N<sub>4</sub>. (C) In situ XANES spectra of Cu<sub>1</sub>@n-C<sub>3</sub>N<sub>4</sub>-27% measured at 0, -0.5, -0.75, and -1 V, with CO as the reactant gas and 1 M KOH as the electrolyte. (D) Plot of partial current density for acetate versus P<sub>CO</sub> at -0.6 V. (E) FEs of CO reduction products measured in dependence of P<sub>CO</sub>, catalyzed by Cu<sub>1</sub>@n-C<sub>3</sub>N<sub>4</sub>-27% at -0.6 V. (F) Kinetic plots showing the reaction order of acetate production with respect to CO. (G) Tafel plots at high-P<sub>CO</sub> (1 atm) and low-P<sub>CO</sub> (0.15 atm) conditions. (H) EXAFS spectra of Cu<sub>1</sub>@n-C<sub>3</sub>N<sub>4</sub>-27% measured at 0, -0.5, -0.75, and -1 V, with CO as the reactant gas and 1 M KOH as the electrolyte. In (C) and (H), the spectra of Cu, Cu<sub>2</sub>O, CuO, and pristine Cu<sub>1</sub>@n-C<sub>3</sub>N<sub>4</sub>-27% (recorded ex situ) are overlapped for comparison. (I) Illustration of the two RDS sceneries associated with the E-R type of C-C coupling mechanism.

\*COH), via



Hereby it should be noticed that the hydrogen is sourced from water molecules instead of coadsorbed \*H, as otherwise one would expect a negative CO reaction order and a lower Tafel slope (21). Because of the strong binding of \*CO (calculated to be 0.94 eV; see the discussion below for computational simulations), the coverage of intermediate adsorbates (\*CO, \*CHO, etc.) on the single-

atom Cu sites is likely not (or weakly) dependent on P<sub>CO</sub>, giving rise to the nearly zero order with respect to CO. At low P<sub>CO</sub>, the scenery with first order and a Tafel slope of -406 mV per decade in combination for acetate production is unprecedented for any known RDS of CO reduction toward C<sub>2+</sub> (table S3), indicating a distinct reaction pathway on the Cu SAECs as compared to the extensively studied metallic Cu electrocatalysts. After more detailed kinetic analysis (see the Supplementary Materials for the details of macrokinetic modeling), we ascribe it to an E-R mechanism on

the single-atom Cu sites



This RDS is a non-Faradaic process and depends weakly on the electrode potential, giving rise to the largely negative Tafel slope (distinct from the electron transfer mediated  $^* \text{CO}$ - $^* \text{CO}$  coupling that has a Tafel slope of ca.  $-120$  mV per decade). Similar to the argument at high  $P_{\text{CO}}$ , the coverage of  $^* \text{CO}$  and its hydrogenated derivatives (including  $^* \text{CHO}$ ) on the single-atom Cu sites is likely high under the reaction conditions, which can be assumed to be independent of the gas-phase concentration of CO even at relatively low  $P_{\text{CO}}$ . Thereby, the RDS (reaction 2) is first order with respect to CO due to the involvement of CO(g).

It should be pointed out that the above two sceneries are not necessarily mutually exclusive and the two steps (reactions 1 and 2) can take place sequentially in a consistent reaction pathway toward  $\text{C}_{2+}$  products (Fig. 4I). The shift of RDS from reactions 1 to 2 at reduced  $P_{\text{CO}}$  can simply be due to the slower rate of the E-R step at low  $P_{\text{CO}}$ , whereas the CO hydrogenation step remains unchanged. As discussed above, such a difference can be ascribed to the strong binding of  $^* \text{CO}$  and saturated coverage of  $^* \text{CO}/^* \text{CHO}$  on the single-atom Cu sites. We also notice that the E-R mechanism described in the RDS (reaction 2) differs from the previously reported C-C coupling mechanism between  $^* \text{CO}$  and CO(g) (51) via



Reaction 3 has been proposed as a possible pathway toward ethylene production on metallic Cu surfaces at high  $P_{\text{CO}}$ , in addition to the C-C coupling between two adjacent  $^* \text{CO}$  (19, 20, 51, 52). This pathway would not give the high- $P_{\text{CO}}$  performance as seen for the Cu SAECs here, although it cannot be excluded for the low- $P_{\text{CO}}$  case. As to be elucidated below, our computational simulations has shown that the formation of  $^* \text{C}_2\text{O}_2$  on the single-atom Cu sites is highly unfavorable, and thereby the pathway via reaction 3 is not considered. On the other side, although a span of SAECs has been reported to produce  $\text{C}_{2+}$  products such as ethylene (53, 54) and ethanol (55), the possible involvement of E-R mechanism for C-C coupling was not explicitly discussed in those studies. As to be discussed below, the Cu SAECs do not only exhibit a unique C-C coupling mechanism, but are also advantageous in its high selectivity toward a specific  $\text{C}_{2+}$  product, reaching  $>50\%$  FE toward acetate. This performance is superior to many Cu-based electrocatalysts relying on the L-H mechanism that usually have broader product distributions [e.g., a multihole cuprous oxide catalyst had only 35% FE toward ethylene as its most selective product, albeit with higher overall FE for  $\text{C}_{2+}$  (56)].

### Computational simulations

To corroborate the reaction pathway derived from the above kinetic analysis, we have performed DFT calculations to simulate the CO reduction pathways on the single-atom Cu sites. Among the various Cu- $\text{N}_x$  configurations ( $x = 2, 3, 6$ ; fig. S22) that are possible for anchoring Cu on the  $g\text{-C}_3\text{N}_4$  substrate, Cu- $\text{N}_2$  with one copper atom coordinated to each unit cell of  $g\text{-C}_3\text{N}_4$  via two Cu-N bonds (fig. S23), at a  $75^\circ$  bonding angle, is predicted to be the energetically most favorable one (fig. S24 and table S4). Noticeably, the formation of fourfold metal-nitrogen coordination (Cu- $\text{N}_4$ ), which is more commonly seen for single metal atoms anchored on nitrogen-

doped carbon substrates (M-N-C) (18, 57–59), is found to be energetically unfavorable on  $g\text{-C}_3\text{N}_4$ , as envisioned from its incompatibility with the threefold symmetry of the  $g\text{-C}_3\text{N}_4$  lattice. Our calculations further show that the oxidation state of Cu in the Cu- $\text{N}_2$  center is +1 (figs. S25 and S26 and table S5). In addition, the dimeric configuration of copper center on the  $g\text{-C}_3\text{N}_4$  substrate (Cu<sub>2</sub>@ $n\text{-C}_3\text{N}_4$ ; fig. S27) was found to be energetically less favorable than the monomers by ca. 0.99 eV. These results are consistent with the experimental characterizations for the Cu<sub>1</sub>@ $n\text{-C}_3\text{N}_4$  catalysts, i.e., Cu(I) anchored on the  $\text{C}_3\text{N}_4$  substrate with a Cu-N coordination number of ca. 2 and no Cu-Cu bonding present (Fig. 2F and table S2). In addition, simulation of possible demetallation processes due to reduction of Cu(I) (59, 60) indicates that the Cu- $\text{N}_2$  center is stable at potentials as negative as  $-1.0$  V versus RHE (fig. S28 and table S6), resembling the high stability of Cu<sub>1</sub>@ $n\text{-C}_3\text{N}_4$  derived from in situ XAS characterizations (Fig. 4, C and H).

CO is shown to bind strongly on the Cu- $\text{N}_2$  site with an adsorption energy of  $-0.94$  eV (table S7). In comparison, the values on Cu(100) and Cu(111) are  $-0.53$  and  $-0.47$  eV, respectively. The much stronger binding of CO on the single-atom Cu sites compared to the metallic copper surfaces is in line with the C=O vibrational feature observed from DRIFTS in the former case but not for the control with Cu nanoparticles (Fig. 4A and fig. S29). It is noted that, in the Cu<sub>1</sub>@ $n\text{-C}_3\text{N}_4$  catalyst, adsorption of CO on the N and C sites adjacent to Cu is not favorable (e.g., 0.24 eV for  $^* \text{CO}$  on C, while  $^* \text{CO}$  on the N site will transfer to the neighboring C site spontaneously; table S8), and, thereby, Cu is likely the only active site accommodating CO adsorption in the SAECs. This finding is also consistent with the observations of single  $^* \text{CO}$  features on the Cu<sub>1</sub>@ $n\text{-C}_3\text{N}_4$  catalyst using DRIFTS (Fig. 4A) and CO stripping (Fig. 4B), but not for the  $g\text{-C}_3\text{N}_4$  substrate. The resolved adsorption properties of Cu<sub>1</sub>@ $n\text{-C}_3\text{N}_4$  thus confirm the atomically dispersed Cu as the active site for CO reduction.

With Cu identified as the active sites, we predict that the electroreduction of CO on Cu<sub>1</sub>@ $n\text{-C}_3\text{N}_4$  starts from CO adsorption and protonation to form  $^* \text{CHO}$  (reaction 1) (Fig. 5 and figs. S31 to S34). Subsequently, C-C coupling via an E-R mechanism (reaction 2) takes place between the  $^* \text{CHO}$  adsorbing on Cu and another gas-phase CO molecule (or dissolved in the electrolyte) to form a  $^* \text{CO-CHO}$ . This  $\text{C}_2$  intermediate is further hydrogenated to form  $^* \text{CO-CHOH}$ ,  $^* \text{CHCO}$ , and  $^* \text{CH}_2\text{CO}$ , sequentially. Eventually,  $^* \text{CH}_2\text{CO}$  could react with a water molecule to produce acetic acid or with an OH<sup>-</sup> to form acetate (Fig. 5, A and B). The  $^* \text{CHO-CO}(\text{g})$  coupling step has a kinetic barrier of 0.80 eV (see fig. S31A), which is comparable to that for the C-C coupling via the L-H mechanism on Cu surfaces (20, 59). This value is also slightly lower than that [0.83 eV with water as the hydrogen source (21); fig. S35] for the hydrogenation of  $^* \text{CO}$  to  $^* \text{CHO}$  on the single-atom Cu sites. The latter, i.e., reaction 1, involves proton coupled electron transfer and turns out to be the RDS for the overall free-energy reaction coordinate to acetate, which agrees with the finding derived from kinetic analysis for high- $P_{\text{CO}}$  conditions. The transition of RDS from CO hydrogenation at high  $P_{\text{CO}}$  to C-C coupling at low  $P_{\text{CO}}$  can be understood via the increase in free energy barrier at reduced  $P_{\text{CO}}$  (fig. S32). The alternative  $^* \text{CO} + \text{CO}(\text{g})$  coupling path (reaction 3), in which the C-C coupling occurs before the protonation of CO, is predicted to have a free-energy barrier of 2.21 eV, much higher than those for the  $^* \text{CHO} + \text{CO}(\text{g})$  coupling and the protonation of  $^* \text{CO}$  and is thus considered to be unfavorable on the Cu SAECs (fig. S34).

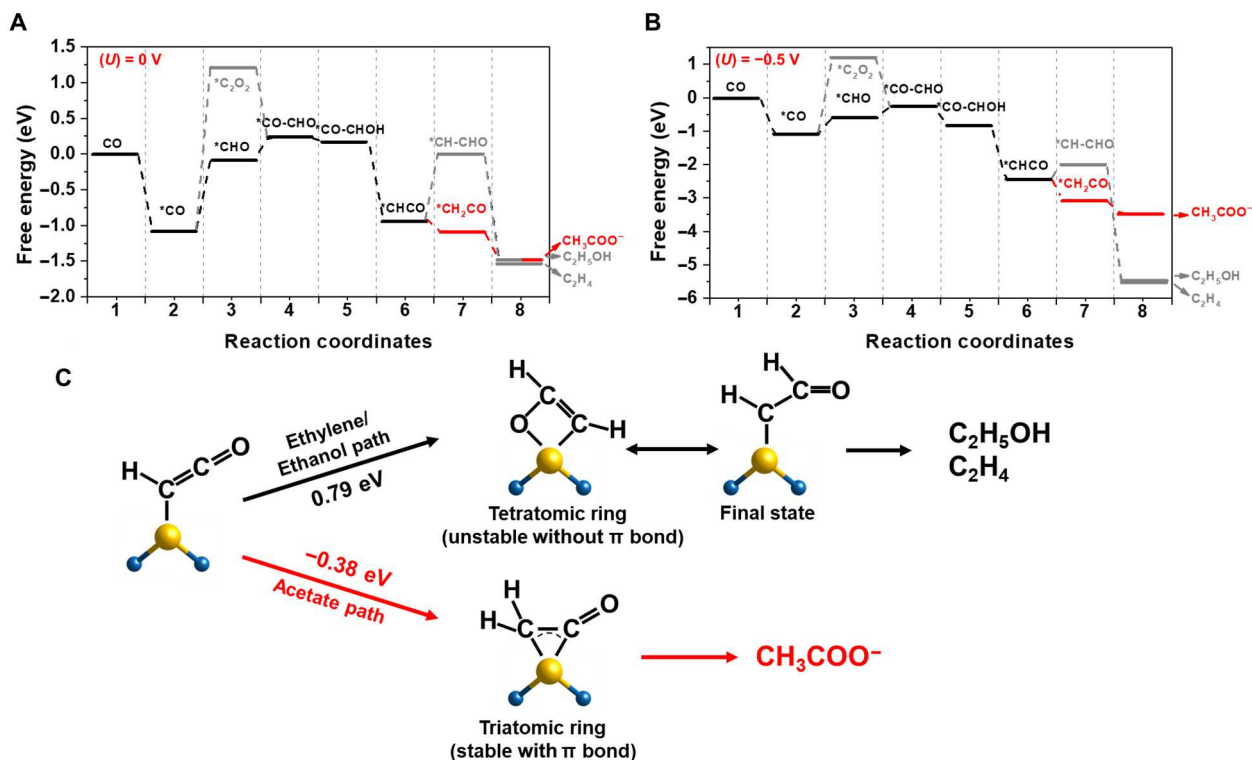


**Fig. 5. Computational simulations.** Predicted free energy evolution for CO reduction to  $C_2$  hydrocarbons on the Cu–N<sub>2</sub> site under an electrode potential of (A) 0 V/RHE and (B) –0.5 V/RHE. (C) Calculated free energy change for \*CH–CO to \*CH<sub>2</sub>CO/\*CH–CHO.

The E–R mechanism described above is believed to be more favorable than possible L–H type of C–C coupling on the Cu<sub>1</sub>@*n*-C<sub>3</sub>N<sub>4</sub> catalyst. Coadsorption of two C<sub>1</sub> species, such as \*CO and/or \*CHO, on a single Cu site is highly unstable with a positive adsorption energy of 0.25 eV (table S9). The activation energy for C–C coupling via the L–H mechanism (\*CO + \*CHO → \*COCHO) is calculated to be 2.45 eV, unsurmountable at room temperature, suggesting that the C–C coupling unlikely goes through the L–H mechanism on the Cu<sub>1</sub>@*n*-C<sub>3</sub>N<sub>4</sub> electrocatalysts (fig. S31B). This is distinct from the case on metallic Cu surfaces, where the continual surface is essential for accommodation of the L–H type of C–C coupling mechanism between neighboring adsorbates (20, 61). We note that the free energies of \*CHO adsorbing on the single-atom Cu site and its adjacent C site are quite similar, which are calculated to be –0.09 and 0.00 eV, respectively (table S9), invoking the possible migration of \*CHO from the former to the latter (62). However, the smallest distance between the \*CHO adsorbing on C and the \*CO on Cu is found to be about 3.8 Å, quite larger than any value known for C–C coupling [e.g., ~3.3 Å for \*CO–\*CO coupling on Cu(100); see fig. S30 for the details of modeling]. In addition to this concern, the reaction order with respect to CO is expected to be nearly zero at low *P*<sub>CO</sub> for the pathway with C–C coupling between \*CO on Cu and \*CHO on C, considering the strong binding of \*CO on the single-atom Cu sites. This would not be consistent with the first order derived from experimental measurements (Fig. 4F). Thereby, the L–H type of C–C coupling mechanism can be excluded for the electroreduction of CO on the Cu SAECs.

After determining the C–C coupling mechanism, we further examined the bifurcation of reaction pathway toward different C<sub>2</sub> products. The continual reduction of \*CHCO can form either \*CH<sub>2</sub>CO or \*CHCHO (Fig. 5, A and B). It has previously been reported that, during the electroreduction of CO, \*CH<sub>2</sub>CO is the intermediate toward acetic acid, whereas \*CHCHO mainly leads to ethylene or ethanol (19, 34). On the Cu–N<sub>2</sub> site, the selectivity toward different C<sub>2</sub> products is determined by the free energy change of two competing reactions, \*CH–CO → \*CH<sub>2</sub>CO toward acetate and \*CH–CO → \*CHCHO toward ethylene and ethanol. After including the solvation effect in our calculations, we predict that the free energies change to be –0.15 eV for the \*CH–CO → \*CH<sub>2</sub>CO step and 0.94 eV for \*CH–CO → \*CHCHO at *U* = 0 V (Fig. 5A), with the former being more favorable by >1 eV than the latter, but both are independent of *P*<sub>CO</sub> on the strongly binding single-atom Cu sites. It should be noted that, while \*CHCHO binds to the Cu–N<sub>2</sub> site via a single C–Cu bond, \*CH<sub>2</sub>CO coordinates onto the single copper-atom site via two C–Cu bonds, forming a three-membered ring with Cu via a π bond (Fig. 5C). Both the π bond and the three-membered ring configuration are believed to be crucial for the stabilization of \*CH<sub>2</sub>CO on the Cu–N<sub>2</sub> site. This is in contrast to the case on metallic copper surfaces, where \*CH–CHO is thermodynamically much more stable on Cu(100) than \*CH<sub>2</sub>CO, causing more favorable formation of ethylene (table S10) (19). In that case, the O atom in \*CH–CHO could coadsorb on the neighboring Cu site to form a five-membered ring, which is an energetically favorable structure (fig. S30). On the single-atom Cu without neighboring coadsorption sites, \*CH–CHO can only form an unstable tetratomic ring, which spontaneously

transforms into the state with a single C—Cu bond (Fig. 5C). Over the course of CO reduction on Cu<sub>1</sub>@*n*-C<sub>3</sub>N<sub>4</sub>, higher *P*<sub>CO</sub> makes the C—C coupling via the E-R mechanism \*CHO + CO(g) → \*COCHO more favorable and thus gives rise to higher reactivity toward C<sub>2</sub> products, but the increase would mainly go toward acetate due to the dominance of \*CH-CO → \*CH<sub>2</sub>CO over \*CH-CO → \*CHCOH toward ethylene. It thus explains the experimentally observed strong dependence of *J*<sub>acetate</sub> on the *P*<sub>CO</sub> but not for *J*<sub>ethylene</sub> (Fig. 4G).

## DISCUSSION

In summary, we have revealed a new C—C coupling mechanism for the electroreduction of CO on single-atom Cu electrocatalysts, Cu<sub>1</sub>@*n*-C<sub>3</sub>N<sub>4</sub>. This type of catalyst contains Cu(I)-N<sub>2</sub> active centers, on which E-R type of C—C coupling takes place between \*CHO (formed via hydrogenation of \*CO strongly binding on Cu) and gas-phase CO. This E-R mechanism can explain the observed catalytic activity and selectivity enhancements, as well as reaction kinetics in terms of reaction order with respect to CO and Tafel slope for acetate production. Moreover, we have also determined the relative stabilities of different C<sub>2</sub> intermediates post C—C coupling on the single-atom Cu site, which explains the high selectivity toward acetate versus other C<sub>2</sub> hydrocarbons. Our work illustrates the great potential of SAECS for the development of CO<sub>2</sub> and CO reduction electrocatalysts beyond Cu metal.

## MATERIALS AND METHODS

### Experimental methods

#### Materials

Copper(II) chloride (CuCl<sub>2</sub>, ≥99.995%), urea (99.0 to 100.5%), potassium hydroxide (KOH) [for cyclic voltammograms (CVs), 99.99%], Nafion 117 containing solution (~5% in a mixture of lower aliphatic alcohols and water), and carbon-<sup>13</sup>C monoxide (<sup>13</sup>CO; <5 atom % of <sup>18</sup>O and 99 atom % of <sup>13</sup>C) were purchased from Sigma-Aldrich. Potassium hydroxide (KOH; for electrolysis, 85% min; K<sub>2</sub>CO<sub>3</sub>, 2.0% max) was purchased from Alfa Aesar. Gas diffusion layer (GDL; Sigracet 39 BCE) and anion exchange membrane (Fumasep FAB-PK-130) were purchased from Fuel Cell Store. All the materials were used without further purification. Electrolyte solutions were prepared using 18.2 megohms of H<sub>2</sub>O (Elga Veolia).

#### Characterization

TEM images were acquired on a Phillips EM 420 microscope. STEM images and EELS were acquired in an aberration-corrected FEI Titan transmission electron microscope operated at a primary electron energy of 300 keV. The microscope is equipped with a probe spherical-aberration corrector that allows for a ~0.1 nm spatial resolution, as well as a Wien-filter monochromator that provides an energy resolution of ~0.3 eV. EELS was acquired using a spectral dispersion of 0.2 eV per channel for the spectrometer. A convergence semiangle of 13.7 mrad is used for both STEM imaging and EELS. For EELS, a collection semiangle of 8.3 mrad is used. For HAADF-STEM imaging, a 70 mrad collection inner angle is used. Elemental and atomic % distribution maps were extracted from EELS spectrum images. Digital Micrograph (Gatan Inc., USA) is used for data acquisition and processing. The XRD data were collected on a laboratory Bruker D8 Focus diffractometer (40 kV, 40 mA, sealed Cu x-ray tube, Ka1 = 1.540596 Å and Ka2

= 1.544493 Å) with a Ni filter and LynxEye position-sensitive detector at room temperature. Gas product was analyzed on-line using a gas chromatography–mass spectrometer (GCMS-QP2010SE, Shimadzu). The liquid product was collected for each potential and analyzed by a 300 MHz nuclear magnetic resonance (NMR) spectrometer (Bruker), with dimethyl sulfoxide as internal standards.

#### Synthesis of Cu<sub>1</sub>@*n*-C<sub>3</sub>N<sub>4</sub>

In typical synthesis of Cu<sub>1</sub>@*n*-C<sub>3</sub>N<sub>4</sub>, 10 g of urea and 268 mg of CuCl<sub>2</sub>·2H<sub>2</sub>O were dissolved in 20 ml of deionized water, and the solution was stirred for 1 hour and dried at 80°C for 12 hours to remove water. The dried mixture was calcined at 550°C for 2 hours with a ramping rate of 25°C/min under a high purity argon (≥99.999%) atmosphere. After pyrolysis, a dark-yellow powder derived was used directly for characterization and catalysis test without acid leaching. The resulting powder was referred to as Cu<sub>1</sub>@*n*-C<sub>3</sub>N<sub>4</sub>–27%. Additional product was obtained with the amount of CuCl<sub>2</sub>·2H<sub>2</sub>O changed to 67 mg, while the other conditions remain the same, and the obtained product was referred to as Cu<sub>1</sub>@*n*-C<sub>3</sub>N<sub>4</sub>–10%. Last, a product synthesized without a copper salt while the other conditions remain the same was referred to as C<sub>3</sub>N<sub>4</sub>.

To synthesize Cu cluster-loaded C<sub>3</sub>N<sub>4</sub>, 50 mg of CuCl<sub>2</sub>·2H<sub>2</sub>O and 50 mg of C<sub>3</sub>N<sub>4</sub> were added to 10 ml of deionized water, sonicated for 5 min, and stirred for 1 hour to obtain a stock solution A. Twenty-two milligrams of NaBH<sub>4</sub> was dissolved in 10 ml of deionized water to form a stock solution B. After that, the stock solution B was added dropwise to stock solution A, and the stirring was continued for 1 hour, followed by centrifugation, washing with deionized water three times, and vacuum-drying at 50°C for 12 hours. The product was referred to as Cu clusters, C<sub>3</sub>N<sub>4</sub>.

#### Electrocatalytic studies

The catalyst ink was prepared from a mixture of catalyst (20 mg), deionized H<sub>2</sub>O (2 ml), isopropanol (2 ml), and Nafion solution (0.15 ml). The mixture was sonicated for at least an hour to form a uniformed suspension. Working electrodes were prepared by drop-casting 0.4 ml of catalyst ink onto the GDL (~1 cm<sup>2</sup>) and wait until it is dry at ambient conditions. Electrochemical measurements were performed using an Autolab 302 potentiostat (Metrohm). A Hg/HgO electrode (Koslow Scientific) was used as the reference electrode. IrO<sub>2</sub> powder deposited on GDLs was used as the counter electrode. Alkaline electrolytes (1 M KOH) were flown through both the cathodic and anodic compartments of the GDE cell at 0.5 ml/min using a syringe pump. CO gas is introduced into the gas chamber at a constant rate of 20 standard cubic centimeters per minute. The gas-phase products were analyzed online using gas chromatograph–mass spectrometry (GC-MS-QP2010SE, Shimadzu), and liquid-phase products were analyzed after ~12 min of reaction at each potential using NMR spectroscopy. All potentials discussed in this work were converted to the RHE scale by following the equation *E* (versus RHE) = *E* (versus Hg/HgO) + 0.14 V + 0.0591 V × pH. The electrochemical test was done with iR correction. A scheme showing the electrochemical setup was included in fig. S21.

CO stripping voltammetry was measured with a rotating disk electrode. For a typical experiment, a catalyst ink, consisting of 1 mg of catalyst, 0.9 ml of deionized H<sub>2</sub>O, 0.1 ml of isopropanol, and 5 μl of Nafion solution, was prepared. A drop of 20 μl of catalyst ink was pipetted onto the glassy carbon electrode and wait until it is

dry. Before the cyclic voltammetry test, the electrode was held at 0.05 V (versus RHE), while pure CO gas was purged into the electrolyte (0.1 M KOH) for 10 min. Then, the electrolyte was purged with Ar gas for 40 min to remove the CO dissolved in the electrolyte. CVs were recorded between 0.05 and 1.05 V (versus RHE) at 50 mV/s.

### CO DRIFTS

Fourier transform infrared spectra for CO adsorption were recorded on a Nicolet 6700 spectrometer equipped with a mercury cadmium telluride detector cooled by liquid N<sub>2</sub>. Before CO adsorption, samples were evacuated at 200°C for 2 hours and then cooled to 25°C for CO adsorption. The DRIFTS spectra were collected at 25°C, after a 30-min purging with Ar. The spectra were collected with a resolution of 4 cm<sup>-1</sup> and accumulation of 100 scans for each sample.

### X-ray absorption spectroscopy

In situ XAS experiments were performed at the 10-BM beamline at the Advanced Photon Source at Argonne National Laboratory. All measurements were performed at the Cu K edge (8.979 keV) in transmission mode in fast scan from 250 eV below the edge to 550 eV above the edge, which took approximately 10 min per scan. The XANES energies were calibrated using Cu foil and set to be 8.8932 eV (table S2). Samples were pressed into a stainless-steel sample holder and placed in a sample cell. The cell was sealed and transferred to the beamline for measurement. At the Cu K edge, the Cu–N (CN = 1, R = 2.1 Å) scattering pair was simulated. S<sub>0</sub><sup>2</sup> was calibrated by fitting the foil. This value was found to be 0.85. A least squared fit the first shell of r-space and isolated q-space were performed on the k<sup>2</sup> weighted Fourier transform data over the range 2.7 to 10 Å<sup>-1</sup> in each spectrum to fit the magnitude and imaginary components. The pre-edge feature at 8.978 eV (Fig. 1E) is a result of s-p hybridization in transition metals and can be attributed to the s → d electron transition of Cu<sup>2+</sup>.

### In situ XAS

A laboratory-made acrylic kit was used for the in situ x-ray measurements (63). In situ XAS measurements of Cu K edge were conducted with the fluorescence mode, in the 7-BM beamline at National Synchrotron Light Source II at Brookhaven National Laboratory. Before the in situ XAS study, the pristine Cu<sub>1</sub>@n-C<sub>3</sub>N<sub>4</sub>-27% was measured as a reference. KOH (1 M) was used as electrolyte and 5% CO (95% Ar) was used as gas reactant. Four cathodic potentials were investigated, 0, -0.5, -0.75, and -1 V (versus RHE). The spectrum of Cu foil was recorded to calibrate the edge energy (E<sub>0</sub>) of the samples under the same experiment conditions. For each sample, 50 scans (30 to 34 s each) were averaged together. The sample was under reaction conditions for 25 to 30 min, and all 50 scans were identical.

### X-ray photoelectron spectroscopy

XPS measurements were analyzed using a Kratos Analytical AXIS Ultra DLD spectrometer. The analyzing chamber of the spectrometer typically maintained an ultrahigh vacuum working pressure below 3.6 × 10<sup>-7</sup> Pa. Spectra were collected using a monochromatic Al Kα x-ray source with 20 eV analyzer pass energy and a 0.7 mm × 0.3 mm spot size. Spectra were evaluated using Casa XPS software.

### Computational methods

The first-principles DFT (64, 65) calculations with plane wave basis set were performed using the Vienna ab initio simulation package (VASP) software (66, 67). The projector augmented wave (68, 69)

pseudo-potential was used to describe the core electrons. The cutoff energies of plane wave basis set were set as 400, 400, and 500 eV to expand the wave functions for CuPc molecule, CuN<sub>2</sub> site, and metallic Cu surface, respectively. The generalized gradient approximation of the revised Perdew, Burke, and Ernzerhof (RPBE) (70) functionals was used to describe the electronic exchange and correlation energy term. The aqueous environment of the electrolyte was treated with a continuum dielectric model as implemented by the Hennig group in the VASP code (71). The relative permittivity was set as 78.4 to model the water environment. CuN<sub>2</sub> moieties embedded in a carbon nitride (C<sub>3</sub>N<sub>4</sub>) layer, p(2 × 2) Cu(100), and p(2 × 2) Cu(111) were modeled as the active sites to catalyze CO reduction reaction. The bond length of Cu–Cu in bulk Cu was predicted to be 2.60 Å. A rhombic C<sub>3</sub>N<sub>4</sub>-layered structure was modeled using 14 atoms, including six carbon atoms and eight nitrogen atoms, and with a lattice parameter of a = b = 7.19 Å. In addition, a 20 Å vacuum region was added perpendicularly to the C<sub>3</sub>N<sub>4</sub> layer to separate periodic images. The Brillouin zone was sampled by Monkhorst and Pack (72) 5 × 5 × 1, 5 × 5 × 1, 5 × 5 × 1, 1 × 1 × 1 k-point grid for models of CuN<sub>2</sub> active site, p(2 × 2) Cu(100), p(2 × 2) Cu(111), and Cu-Pc molecule, respectively. Bader charge analysis (73) was used to calculate the total valence electron number of Cu in Cu–N<sub>2</sub> and Cu-Pc.

In structural optimization calculations, the atom positions were relaxed until the force on each ion fell below 0.01 eV/Å. In our molecular vibration frequency calculation of Cu–N<sub>2</sub> site, all the C and N atoms were fixed, whereas the Cu and H atoms were allowed to make vibrational motion. As for the vibrational frequency calculation of molecule in gas phase, all the atoms allow to make vibrational motion. The computational hydrogen electrode was used to calculate the free energy of corresponding reaction intermediates and evaluate the limiting potential of CORR on various active sites. All computations were conducted under electrode potential U = 0 V. The free energy of a chemical reaction was calculated as follows

$$\Delta G = \Delta E_{\text{DFT}} + \Delta E_{\text{ZPE}} + \Delta H_T - T\Delta S$$

where  $\Delta E_{\text{DFT}}$  is the energy change derived from DFT calculation,  $\Delta E_{\text{ZPE}}$  is the zero-point energy change,  $\Delta H_T$  is the enthalpy change from 0 to T K, and  $\Delta S$  is entropy change for the reaction. ZPE corrections were calculated as  $\text{ZPE} = \sum \frac{1}{2} h\nu_i$ , where  $h$  is the Planck's constant and  $\nu_i$  is the frequency of the corresponding vibrational mode of binding molecules. The vibrational heat capacity integration  $\int_0^T C_p(t) dt$  was used to calculate the  $\Delta H_T$ . The entropy term

$$S = k_B * \sum_i \left\{ \frac{h\nu_i}{k_B T} * \frac{1}{\exp\left(\frac{h\nu_i}{k_B T}\right) - 1} - \ln \left[ 1 - \exp\left(-\frac{h\nu_i}{k_B T}\right) \right] \right\}, \text{ where } T \text{ is}$$

the temperature of reaction,  $S$  is the vibrational entropy,  $h$  is the Planck's constant,  $k_B$  is the Boltzmann constant, and  $\nu_i$  is the frequency of the  $i$ th vibrational mode.

For the molecules, the free energies were calculated as follow

$$G = E_{\text{DFT}} + E_{\text{ZPE}} + H_T - TS + \frac{n}{2} k_B T$$

where  $n$  is eight for nonlinear molecule and seven for linear molecule. We adopted the implicit solvation model to predict the free energy of CH<sub>3</sub>COO<sup>-</sup> and C<sub>2</sub>H<sub>5</sub>OH in aqueous solution. The free

energy correction for molecule in aqueous solution was predicted to be  $-0.18$  eV for  $C_2H_5OH$ , and  $-0.32$  eV for  $CH_3COO^-$ , respectively.

#### Validation of CO adsorption on Cu(111)/Cu(100) surface using RPBE functional

In experiment, the measured CO coverage on Cu(100) or Cu(111) surface was reported to be higher than 0.25 (74). To validate our DFT method using the experimental result, we constructed a  $p(2 \times 2)$  Cu(100) and Cu(111) surfaces with a CO molecule (coverage of 0.25) adsorbed on and predicted the corresponding CO adsorption energies to be  $-0.53$  eV on Cu(100) surface and  $-0.47$  eV on Cu(111) (table S7). These predictions agrees well with experimentally measured CO adsorption energies of  $-0.53$  eV on Cu(100) surface and  $-0.49$  eV on Cu(111) (74). This result suggests that RPBE shows accurate prediction for CO adsorption on Cu surface, in line with the conclusion of previous work (75).

#### Calculations for energy barrier/activation energy

Moreover, the constrained ab initio molecular dynamics (AIMD) calculation (76) with reaction coordination gradually changing from the initial to the final state (slow growth method) was applied to predict the activation energy for the C–C coupling reaction via the E-R mechanism at 300 K. The simulation was conducted using the canonical ensemble without considering the interaction between CO molecules. Nose-Hoover thermostat was used to keep temperature constant at 300 K (77). Time step in AIMD was set to be 1 fs. As shown in fig. S31A, we predicted the activation energy for C–C coupling via E-R mechanism to be 0.80 eV.

In addition, the nudged elastic band (NEB) calculations (78) were performed to identify the transition state and predict the activation energy for the C–C coupling reaction via the L-H mechanism and CO hydrogenation reaction. In NEB calculation, the force along and perpendicular to the reaction path was relaxed to less than  $0.05$  eV/Å. The activation energy for C–C coupling via L-H mechanism was predicted to be 2.45 eV (fig. S31B). In addition, the activation energies for CO hydrogenation were predicted to be 0.55 eV using proton as the hydrogen source and 0.83 eV using water as the hydrogen source, respectively (fig. S35 and note S2).

#### Calculations for methane pathway

The bifurcation step between methane pathway and C2 product pathway on Cu- $C_3N_4$  site is as follows (fig. S32). Following the methane pathway, the adsorbed CHO will be protonated to form \*CHOH, whereas the adsorbed CHO will be coupled with other CO to form \*CO-CHO through C2 product pathway. We predicted the free energy change for \*CHO  $\rightarrow$  \*CHOH step to be 0.55 eV, higher than that of 0.22 eV for CHO-CO coupling step. This result indicates that CHO-CO coupling reaction is more thermodynamically favorable than CHO protonation, explaining the high C2 product selectivity on Cu- $C_3N_4$  site. Moreover, we predicted the free energy change to be  $-0.15$  eV for \*CH-CO  $\rightarrow$  \*CH<sub>2</sub>CO step and 0.94 eV for \*CH-CO  $\rightarrow$  \*CHCOH step. This result further reveals that acetate pathway is more favorable than ethylene or ethanol pathway.

### Supplementary Materials

This PDF file includes:

Tables S1 to S12

Figs. S1 to S35

Supplementary Text

### REFERENCES AND NOTES

- D. T. Whipple, P. J. A. Kenis, Prospects of CO<sub>2</sub> utilization via direct heterogeneous electrochemical reduction. *J. Phys. Chem. Lett.* **1**, 3451–3458 (2010).
- P. De Luna, C. Hahn, D. Higgins, S. A. Jaffer, T. F. Jaramillo, E. H. Sargent, What would it take for renewably powered electrosynthesis to displace petrochemical processes? *Science* **364**, eaav3506 (2019).
- H. Xiao, T. Cheng, W. A. Goddard, R. Sundararaman, Mechanistic explanation of the pH dependence and onset potentials for hydrocarbon products from electrochemical reduction of CO on Cu (111). *J. Am. Chem. Soc.* **138**, 483–486 (2016).
- C. T. Dinh, T. Burdyny, M. G. Kibria, A. Seifitokaldani, C. M. Gabardo, F. P. G. de Arquer, A. Kiani, J. P. Edwards, P. De Luna, O. S. Bushuyev, C. Q. Zou, R. Quintero-Bermudez, Y. J. Pang, D. Sinton, E. H. Sargent, CO<sub>2</sub> electroreduction to ethylene via hydroxide-mediated copper catalysis at an abrupt interface. *Science* **360**, 783–787 (2018).
- J. A. Rabinowitz, M. W. Kanan, The future of low-temperature carbon dioxide electrolysis depends on solving one basic problem. *Nat. Commun.* **11**, 5231 (2020).
- Y. Hori, H. Wakebe, T. Tsukamoto, O. Koga, Electrocatalytic process of CO selectivity in electrochemical reduction of CO<sub>2</sub> at metal electrodes in aqueous media. *Electrochim. Acta* **39**, 1833–1839 (1994).
- B. A. Rosen, A. Salehi-Khojin, M. R. Thorson, W. Zhu, D. T. Whipple, P. J. A. Kenis, R. I. Masel, Ionic liquid-mediated selective conversion of CO<sub>2</sub> to CO at low overpotentials. *Science* **334**, 643–644 (2011).
- K. J. P. Schouten, Z. Qin, E. Pérez Gallent, M. T. M. Koper, Two pathways for the formation of ethylene in CO reduction on single-crystal copper electrodes. *J. Am. Chem. Soc.* **134**, 9864–9867 (2012).
- S. Ma, M. Sadakiyo, M. Heima, R. Luo, R. T. Haasch, J. I. Gold, M. Yamauchi, P. J. A. Kenis, Electroreduction of carbon dioxide to hydrocarbons using bimetallic Cu–Pd catalysts with different mixing patterns. *J. Am. Chem. Soc.* **139**, 47–50 (2017).
- M. Jouny, W. Luc, F. Jiao, High-rate electroreduction of carbon monoxide to multi-carbon products. *Nat. Catal.* **1**, 748–755 (2018).
- D. Raciti, C. Wang, Electrochemical alternative to Fischer–Tropsch. *Nat. Catal.* **1**, 741–742 (2018).
- J. Li, Z. Wang, C. McCallum, Y. Xu, F. Li, Y. Wang, C. M. Gabardo, C.-T. Dinh, T.-T. Zhuang, L. Wang, J. Y. Howe, Y. Ren, E. H. Sargent, D. Sinton, Constraining CO coverage on copper promotes high-efficiency ethylene electroproduction. *Nat. Catal.* **2**, 1124–1131 (2019).
- H. Mistry, R. Reske, Z. Zeng, Z.-J. Zhao, J. Greeley, P. Strasser, B. R. Cuenya, Exceptional size-dependent activity enhancement in the electroreduction of CO<sub>2</sub> over Au nanoparticles. *J. Am. Chem. Soc.* **136**, 16473–16476 (2014).
- C. G. Morales-Guio, E. R. Cave, S. A. Nitopi, J. T. Feaster, L. Wang, K. P. Kuhl, A. Jackson, N. C. Johnson, D. N. Abram, T. Hatsukade, C. Hahn, T. F. Jaramillo, Improved CO<sub>2</sub> reduction activity towards C<sub>2+</sub> alcohols on a tandem gold on copper electrocatalyst. *Nat. Catal.* **1**, 764–771 (2018).
- S. Mezzavilla, S. Horch, I. E. L. Stephens, B. Seger, I. Chorkendorff, Structure sensitivity in the electrocatalytic reduction of CO<sub>2</sub> with gold catalysts. *Angew. Chem. Int. Ed.* **58**, 3774–3778 (2019).
- Q. Lu, J. Rosen, Y. Zhou, G. S. Hutchings, Y. C. Kimmel, J. G. Chen, F. Jiao, A selective and efficient electrocatalyst for carbon dioxide reduction. *Nat. Commun.* **5**, 3242 (2014).
- T. Zheng, K. Jiang, N. Ta, Y. Hu, J. Zeng, J. Liu, H. Wang, Large-scale and highly selective CO<sub>2</sub> electrocatalytic reduction on nickel single-atom catalyst. *Joule* **3**, 265–278 (2019).
- Y. Wang, H. Su, Y. He, L. Li, S. Zhu, H. Shen, P. Xie, X. Fu, G. Zhou, C. Feng, D. Zhao, F. Xiao, X. Zhu, Y. Zeng, M. Shao, S. Chen, G. Wu, J. Zeng, C. Wang, Advanced electrocatalysts with single-metal-atom active sites. *Chem. Rev.* **120**, 12217–12314 (2020).
- F. Calle-Vallejo, M. T. M. Koper, Theoretical considerations on the electroreduction of CO to C<sub>2</sub> species on Cu(100) electrodes. *Angew. Chem. Int. Ed.* **52**, 7282–7285 (2013).
- J. H. Montoya, C. Shi, K. Chan, J. K. Norskov, Theoretical insights into a CO dimerization mechanism in CO<sub>2</sub> electroreduction. *J. Phys. Chem. Lett.* **6**, 2032–2037 (2015).
- T. Cheng, H. Xiao, W. A. Goddard, Full atomistic reaction mechanism with kinetics for CO reduction on Cu(100) from ab initio molecular dynamics free-energy calculations at 298 K. *Proc. Natl. Acad. Sci. U.S.A.* **114**, 1795–1800 (2017).
- A. J. Garza, A. T. Bell, M. Head-Gordon, Mechanism of CO<sub>2</sub> reduction at copper surfaces: Pathways to C<sub>2</sub> products. *ACS Catal.* **8**, 1490–1499 (2018).
- Y. Pang, J. Li, Z. Wang, C.-S. Tan, P.-L. Hsieh, T.-T. Zhuang, Z.-Q. Liang, C. Zou, X. Wang, P. De Luna, J. P. Edwards, Y. Xu, F. Li, C.-T. Dinh, M. Zhong, Y. Lou, D. Wu, L.-J. Chen, E. H. Sargent, D. Sinton, Efficient electrocatalytic conversion of carbon monoxide to propanol using fragmented copper. *Nat. Catal.* **2**, 251–258 (2019).
- M. Jouny, G. S. Hutchings, F. Jiao, Carbon monoxide electroreduction as an emerging platform for carbon utilization. *Nat. Catal.* **2**, 1062–1070 (2019).
- D. Raciti, C. Wang, Recent advances in CO<sub>2</sub> reduction electrocatalysis on copper. *ACS Energy Lett.* **3**, 1545–1556 (2018).

26. S. Nitopi, E. Bertheussen, S. B. Scott, X. Liu, A. K. Engstfeld, S. Horch, B. Seger, I. E. L. Stephens, K. Chan, C. Hahn, J. K. Nørskov, T. F. Jaramillo, I. Chorkendorff, Progress and perspectives of electrochemical CO<sub>2</sub> reduction on copper in aqueous electrolyte. *Chem. Rev.* **119**, 7610–7672 (2019).
27. A. Loidice, P. Lobaccaro, E. A. Kamali, T. Thao, B. H. Huang, J. W. Ager, R. Buonsanti, Tailoring copper nanocrystals towards C<sub>2</sub> products in electrochemical CO<sub>2</sub> reduction. *Angew. Chem. Int. Ed.* **55**, 5789–5792 (2016).
28. E. Pérez-Gallent, M. C. Figueiredo, F. Calle-Vallejo, M. T. M. Koper, Spectroscopic observation of a hydrogenated CO dimer intermediate during CO reduction on Cu(100) electrodes. *Angew. Chem. Int. Ed.* **56**, 3621–3624 (2017).
29. J. D. Goodpaster, A. T. Bell, M. H. Head-Gordon, Identification of possible pathways for C–C bond formation during electrochemical reduction of CO<sub>2</sub>: New theoretical insights from an improved electrochemical model. *J. Phys. Chem. Lett.* **7**, 1471–1477 (2016).
30. T. Cheng, H. Xiao, W. A. Goddard, Free-energy barriers and reaction mechanisms for the electrochemical reduction of CO on the Cu(100) surface, including multiple layers of explicit solvent at pH 0. *J. Phys. Chem. Lett.* **6**, 4767–4773 (2015).
31. D. Raciti, L. Cao, K. J. T. Livi, P. F. Rottmann, X. Tang, C. Li, Z. Hicks, K. H. Bowen, K. J. Hemker, T. Mueller, C. Wang, Low-overpotential electroreduction of carbon monoxide using copper nanowires. *ACS Catal.* **7**, 4467–4472 (2017).
32. K. J. P. Schouten, E. Pérez Gallent, M. T. M. Koper, The influence of pH on the reduction of CO and CO<sub>2</sub> to hydrocarbons on copper electrodes. *J. Electroanal. Chem.* **716**, 53–57 (2014).
33. D. Raciti, M. Mao, J. H. Park, C. Wang, Local pH effect in the CO<sub>2</sub> reduction reaction on high-surface-area copper electrocatalysts. *J. Electrochem. Soc.* **165**, F799–F804 (2018).
34. W. Luc, X. Fu, J. Shi, J.-J. Lv, M. Jouny, B. Hee Ko, Y. Xu, Q. Tu, X. Hu, J. Wu, Q. Yue, Y. Liu, F. Jiao, Y. Kang, Two-dimensional copper nanosheets for electrochemical reduction of carbon monoxide to acetate. *Nat. Catal.* **2**, 423–430 (2019).
35. X. Liu, P. Schlexer, J. Xiao, Y. Ji, L. Wang, R. B. Sandberg, M. Tang, K. S. Brown, H. Peng, S. Ringe, C. Hahn, T. F. Jaramillo, J. K. Nørskov, K. Chan, pH effects on the electrochemical reduction of CO<sub>2</sub> towards C<sub>2</sub> products on stepped copper. *Nat. Commun.* **10**, 32 (2019).
36. A. A. Peterson, J. K. Nørskov, Activity descriptors for CO<sub>2</sub> electroreduction to methane on transition-metal catalysts. *J. Phys. Chem. Lett.* **3**, 251–258 (2012).
37. J. Liu, T. Zhang, Z. Wang, G. Dawson, W. Chen, Simple pyrolysis of urea into graphitic carbon nitride with recyclable adsorption and photocatalytic activity. *J. Mater. Chem.* **21**, 14398–14401 (2011).
38. L. Zhang, R. Long, Y. Zhang, D. Duan, Y. Xiong, Y. Zhang, Y. Bi, Direct observation of dynamic bond evolution in single-atom Pt/C<sub>3</sub>N<sub>4</sub> catalysts. *Angew. Chem. Int. Ed.* **59**, 6224–6229 (2020).
39. C. G. Schroer, M. Kuhlmann, T. F. Günzler, B. Lengeler, M. Richwin, B. Griesebock, D. Lützenkirchen-Hecht, R. Frahm, E. Ziegler, A. Mashayekhi, D. R. Haefner, J. D. Grunwaldt, A. Baiker, Mapping the chemical states of an element inside a sample using tomographic x-ray absorption spectroscopy. *Appl. Phys. Lett.* **82**, 3360–3362 (2003).
40. J. Jiao, R. Lin, S. Liu, W.-C. Cheong, C. Zhang, Z. Chen, Y. Pan, J. Tang, K. Wu, S.-F. Hung, H. M. Chen, L. Zheng, Q. Lu, X. Yang, B. Xu, H. Xiao, J. Li, D. Wang, Q. Peng, C. Chen, Y. Li, Copper atom-pair catalyst anchored on alloy nanowires for selective and efficient electrochemical reduction of CO<sub>2</sub>. *Nat. Chem.* **11**, 222–228 (2019).
41. L. S. Kau, D. J. Spira-Solomon, J. E. Penner-Hahn, K. O. Hodgson, E. I. Solomon, X-ray absorption edge determination of the oxidation state and coordination number of copper. Application to the type 3 site in *Rhus vernicifera* laccase and its reaction with oxygen. *J. Am. Chem. Soc.* **109**, 6433–6442 (1987).
42. D. T. Whipple, E. C. Finke, P. J. A. Kenis, Microfluidic reactor for the electrochemical reduction of carbon dioxide: The effect of pH. *Electrochem. Solid State Lett.* **13**, B109 (2010).
43. Y. Wang, H. Shen, K. J. T. Livi, D. Raciti, H. Zong, J. Gregg, M. Onadeko, Y. Wan, A. Watson, C. Wang, Copper nanocubes for CO<sub>2</sub> reduction in gas diffusion electrodes. *Nano Lett.* **19**, 8461–8468 (2019).
44. B. Qiao, A. Wang, X. Yang, L. F. Allard, Z. Jiang, Y. Cui, J. Liu, J. Li, T. Zhang, Single-atom catalysis of CO oxidation using Pt<sub>1</sub>/FeO<sub>x</sub>. *Nat. Chem.* **3**, 634–641 (2011).
45. P. Xie, T. Pu, A. Nie, S. Hwang, S. C. Purdy, W. Yu, D. Su, J. T. Miller, C. Wang, Nanoceria-supported single-atom platinum catalysts for direct methane conversion. *ACS Catal.* **8**, 4044–4048 (2018).
46. A. Verdager-Casadevall, C. W. Li, T. P. Johansson, S. B. Scott, J. T. McKeown, M. Kumar, I. E. L. Stephens, M. W. Kanan, I. Chorkendorff, Probing the active surface sites for CO reduction on oxide-derived copper electrocatalysts. *J. Am. Chem. Soc.* **137**, 9808–9811 (2015).
47. Y. Lei, H. Zhao, R. D. Rivas, S. Lee, B. Liu, J. Lu, E. Stach, R. E. Winans, K. W. Chapman, J. P. Greeley, J. T. Miller, P. J. Chupas, J. W. Elam, Adsorbate-induced structural changes in 1–3 nm platinum nanoparticles. *J. Am. Chem. Soc.* **136**, 9320–9326 (2014).
48. D. Friebe, V. Viswanathan, D. J. Miller, T. Anniyev, H. Ogasawara, A. H. Larsen, C. P. O’Grady, J. K. Nørskov, A. Nilsson, Balance of nanostructure and bimetallic interactions in Pt model fuel cell catalysts: In situ XAS and DFT study. *J. Am. Chem. Soc.* **134**, 9664–9671 (2012).
49. J. Li, K. Chang, H. Zhang, M. He, W. A. Goddard, J. G. Chen, M.-J. Cheng, Q. Lu, Effectively increased efficiency for electroreduction of carbon monoxide using supported polycrystalline copper powder electrocatalysts. *ACS Catal.* **9**, 4709–4718 (2019).
50. S. Fletcher, Tafel slopes from first principles. *J. Solid State Electrochem.* **13**, 537–549 (2009).
51. X. Wang, J. F. de Araújo, W. Ju, A. Bagger, H. Schmies, S. Kühn, J. Rossmel, P. Strasser, Mechanistic reaction pathways of enhanced ethylene yields during electroreduction of CO<sub>2</sub>–CO feeds on Cu and Cu-tandem electrocatalysts. *Nat. Nanotechnol.* **14**, 1063–1070 (2019).
52. T. Cheng, H. Xiao, W. A. Goddard, Nature of the active sites for CO reduction on copper nanoparticles; suggestions for optimizing performance. *J. Am. Chem. Soc.* **139**, 11642–11645 (2017).
53. H. Bao, Y. Qiu, X. Peng, J.-A. Wang, Y. Mi, S. Zhao, X. Liu, Y. Liu, R. Cao, L. Zhuo, J. Ren, J. Sun, J. Luo, X. Sun, Isolated copper single sites for high-performance electroreduction of carbon monoxide to multicarbon products. *Nat. Commun.* **12**, 238 (2021).
54. A. Guan, Z. Chen, Y. Quan, C. Peng, Z. Wang, T.-K. Sham, C. Yang, Y. Ji, L. Qian, X. Xu, G. Zheng, Boosting CO<sub>2</sub> electroreduction to CH<sub>4</sub> via tuning neighboring single-copper sites. *ACS Energy Lett.* **5**, 1044–1053 (2020).
55. L. Ji, L. Li, X. Ji, Y. Zhang, S. Mou, T. Wu, Q. Liu, B. Li, X. Zhu, Y. Luo, X. Shi, A. M. Asiri, X. Sun, Highly selective electrochemical reduction of CO<sub>2</sub> to alcohols on an FeP nanoarray. *Angew. Chem. Int. Ed.* **59**, 758–762 (2020).
56. P.-P. Yang, X.-L. Zhang, F.-Y. Gao, Y.-R. Zheng, Z.-Z. Niu, X. Yu, R. Liu, Z.-Z. Wu, S. Qin, L.-P. Chi, Y. Duan, T. Ma, X.-S. Zheng, J.-F. Zhu, H.-J. Wang, M.-R. Gao, S.-H. Yu, Protecting copper oxidation state via intermediate confinement for selective CO<sub>2</sub> electroreduction to C<sub>2+</sub> fuels. *J. Am. Chem. Soc.* **142**, 6400–6408 (2020).
57. F. Pan, H. Zhang, K. Liu, D. Cullen, K. More, M. Wang, Z. Feng, G. Wang, G. Wu, Y. Li, Unveiling active sites of CO<sub>2</sub> reduction on nitrogen-coordinated and atomically dispersed iron and cobalt catalysts. *ACS Catal.* **8**, 3116–3122 (2018).
58. W. Ju, A. Bagger, G.-P. Hao, A. S. Varela, I. Sinev, V. Bon, B. Roldan Cuenya, S. Kaskel, J. Rossmel, P. Strasser, Understanding activity and selectivity of metal-nitrogen-doped carbon catalysts for electrochemical reduction of CO<sub>2</sub>. *Nat. Commun.* **8**, 944 (2017).
59. D. Karapinar, N. T. Huan, N. Ranjbar Sahraie, J. Li, D. Wakerley, N. Touati, S. Zanna, D. Taverna, L. H. Galvão Tizei, A. Zitolo, F. Jaouen, V. Mougél, M. Fontecave, Electroreduction of CO<sub>2</sub> on single-site copper-nitrogen-doped carbon material: Selective formation of ethanol and reversible restructuring of the metal sites. *Angew. Chem. Int. Ed.* **58**, 15098–15103 (2019).
60. Z. Weng, Y. Wu, M. Wang, J. Jiang, K. Yang, S. Huo, X.-F. Wang, Q. Ma, G. W. Brudvig, V. S. Batista, Y. Liang, Z. Feng, H. Wang, Active sites of copper-complex catalytic materials for electrochemical carbon dioxide reduction. *Nat. Commun.* **9**, 415 (2018).
61. H. Li, Y. Li, M. T. M. Koper, F. Calle-Vallejo, Bond-making and breaking between carbon, nitrogen, and oxygen in electrocatalysis. *J. Am. Chem. Soc.* **136**, 15694–15701 (2014).
62. Y. Jiao, Y. Zheng, P. Chen, M. Jaroniec, S.-Z. Qiao, Molecular scaffolding strategy with synergistic active centers to facilitate electrocatalytic CO<sub>2</sub> reduction to hydrocarbon/alcohol. *J. Am. Chem. Soc.* **139**, 18093–18100 (2017).
63. J. H. Lee, S. Kattel, Z. Jiang, Z. Xie, S. Yao, B. M. Tackett, W. Xu, N. S. Marinkovic, J. G. Chen, Tuning the activity and selectivity of electroreduction of CO<sub>2</sub> to synthesis gas using bimetallic catalysts. *Nat. Commun.* **10**, 3724 (2019).
64. P. Hohenberg, W. Kohn, Inhomogeneous electron gas. *Phys. Rev.* **136**, B864–B871 (1964).
65. W. Kohn, L. J. Sham, Self-consistent equations including exchange and correlation effects. *Phys. Rev.* **140**, A1133–A1138 (1965).
66. G. Kresse, J. Hafner, Ab initio molecular dynamics for liquid metals. *Phys. Rev. B* **47**, 558–561 (1993).
67. G. Kresse, J. Furthmüller, Efficiency of ab-initio total energy calculations for metals and semiconductors using a plane-wave basis set. *Comput. Mater. Sci.* **6**, 15–50 (1996).
68. P. E. Blöchl, Projector augmented-wave method. *Phys. Rev. B* **50**, 17953–17979 (1994).
69. G. Kresse, D. Joubert, From ultrasoft pseudopotentials to the projector augmented-wave method. *Phys. Rev. B* **59**, 1758–1775 (1999).
70. B. Hammer, L. B. Hansen, J. K. Nørskov, Improved adsorption energetics within density-functional theory using revised Perdew-Burke-Ernzerhof functionals. *Phys. Rev. B* **59**, 7413–7421 (1999).
71. K. Mathew, R. Sundararaman, K. Letchworth-Weaver, T. Arias, R. G. Hennig, Implicit solvation model for density-functional study of nanocrystal surfaces and reaction pathways. *J. Chem. Phys.* **140**, 084106 (2014).
72. H. J. Monkhorst, J. D. Pack, Special points for Brillouin-zone integrations. *Phys. Rev. B* **13**, 5188–5192 (1976).
73. E. Sanville, S. D. Kenny, R. Smith, G. Henkelman, Improved grid-based algorithm for Bader charge allocation. *J. Comput. Chem.* **28**, 899–908 (2007).

74. S. Vollmer, G. Witte, C. Wöll, Determination of site specific adsorption energies of CO on copper. *Catal. Lett.* **77**, 97–101 (2001).
75. C. N. Lininger, J. A. Gauthier, W.-L. Li, E. Rossomme, V. V. Welborn, Z. Lin, T. Head-Gordon, M. Head-Gordon, A. T. Bell, Challenges for density functional theory: Calculation of CO adsorption on electrocatalytically relevant metals. *Phys. Chem. Chem. Phys.* **23**, 9394–9406 (2021).
76. H. Oberhofer, C. Dellago, P. L. Geissler, Biased sampling of nonequilibrium trajectories: Can fast switching simulations outperform conventional free energy calculation methods? *J. Phys. Chem. B* **109**, 6902–6915 (2005).
77. W. G. Hoover, Canonical dynamics: Equilibrium phase-space distributions. *Phys. Rev. A* **31**, 1695–1697 (1985).
78. G. Henkelman, B. P. Uberuaga, H. Jónsson, A climbing image nudged elastic band method for finding saddle points and minimum energy paths. *J. Chem. Phys.* **113**, 9901–9904 (2000).

#### Acknowledgments

**Funding:** This work is supported by National Science Foundation (CBET-1930013 and CBET-1803482) and Department of Energy (DE-EE0008501). The research used resources of the Center for Functional Nanomaterials (CFN) and the National Synchrotron Light Source II, both are U.S. Department of Energy (DOE) Office of Science user facilities operated for the DOE Office

of Science by Brookhaven National Laboratory under contract no. DE-SC0012704. Beamline operations were supported in part by the Synchrotron Catalysis Consortium, U.S. DOE, Office of Basic Energy Sciences (grant no. DE-SC0012335). **Author contributions:** Y.W. and Chao Wang conceived the concept and drafted the original version of the manuscript. Y.W., B.X., H.S., Canhui Wang, D.R., H.Z., W.X., Z.L., G.Z., and J.V. performed the synthesis, characterization, and electrocatalytic studies. N.L., Z.X., N.M., J.G.C., and J.M. conducted the XAS studies. B.L. and G.W. developed the computational methods and conducted the simulations. All authors approved the final version of manuscript. **Competing interests:** The authors declare that they have no competing interests. Certain commercial equipment, instruments, or materials are identified in this paper to specify the experimental procedure adequately. Such identification is not intended to imply recommendation or endorsement by the National Institute of Standards and Technology, nor is it intended to imply that the materials or equipment identified are necessarily the best available for the purpose. **Data and materials availability:** All data needed to evaluate the conclusions in the paper are present in the paper and/or the Supplementary Materials.

Submitted 10 August 2022

Accepted 22 June 2023

Published 26 July 2023

10.1126/sciadv.ade3557